Article:

Yousef, BM, Almarzooq, H, Angus, DA et al. (1 more author) (2017) Fracture parameter inversion from passive seismic shear-wave splitting: A validation study using full-waveform numerical synthetics. Tectonophysics, 712-71. pp. 736-746. ISSN 0040-1951

https://doi.org/10.1016/j.tecto.2017.06.034

Fracture parameter inversion from passive seismic shear-wave splitting: A validation study using full-waveform numerical synthetics

Yousef[1], B.M., Almarzooq[1], H., Angus[2], D.A. & Hildyard[1], M.W.

1. School of Earth & Environment, University of Leeds, Leeds, UK
2. ESG Solutions, Kingston, Canada

Abstract

Fractures are pervasive features within the Earth's crust and they have a significant influence on the multi-physical response of the subsurface. The presence of coherent fracture sets often leads to observable seismic anisotropy enabling seismic techniques to remotely locate and characterise fracture systems. Since fractures play a critical role in the geomechanical and fluid-flow response, there has been significant interest in quantitatively imaging in situ fractures for improved hydro-mechanical modelling. In this study we assess the robustness of inverting for fracture properties using shear-wave splitting measurements. We show that it is feasible to invert shear-wave splitting measurements to quantitatively estimate fracture strike and fracture density assuming an effective medium fracture model. Although the SWS results themselves are diagnostic of fracturing, the fracture inversion allows placing constraints on the physical properties of the fracture system. For the single seismic source case and optimum receiver array geometry, the inversion for strike has average errors of between 11° and 25°, whereas for density has average errors between 65% and 80% for the single fracture set and 30% and 90% for the double fracture sets. For real microseismic datasets, the range in magnitude of microseismicity (i.e., frequency content), spatial distribution and variable source mechanisms suggests that the inversion of fracture properties from SWS measurements is feasible.

Keywords: explicit fractures, finite-difference, fracture inversion,

full-waveform synthetics, shear-wave splitting

1. Introduction

Fractures are pervasive features within the brittle crust, ranging in size over several orders of magnitude, from large scale faults (km) down to micro-cracks in core samples (mm). Fractures play a critical role in the multi-physical response of Earth materials, influencing the stress and strain fields leading to geomechanical deformation as well as acting as secondary conduits for fluid-flow contributing to fluid movement in porous media. Fractures also influence the geophysical response of the subsurface, such as modifying seismic velocities due to stress-dependent fracture stiffness.

Three-dimensional hydro-mechanical (HM) modelling of subsurface reservoirs has significantly progressed in the past decade to help the petroleum industry efficiently and safely extract hydrocarbons from unconventional reservoirs, such as shale-gas and coal-seam methane, and extreme environments at high-pressures and temperatures. Furthermore, with the recent drive to reduce anthropogenic CO_2 emissions using carbon capture and geo-sequestration, HM modelling is a necessary step to predict risk and storage security. However, HM models need to be calibrated using real physical measurements, such as pore pressures, surface subsidence, and time-lapse and passive seismic monitoring. Since fractures play a critical role in the geomechanical and fluid-flow response, there has been significant interest in quantitatively imaging in situ fractures for improved HM modelling.

The fact that fractures form coherent regions with directional dependence of decreased stiffness leads to observable seismic anisotropy. Seismic anisotropy refers to directional variations in seismic velocities, which in reservoirs is due to intrinsic anisotropy, preferred alignment of sub-seismic scale fractures and the influence of non-hydrostatic changes in the stress field on micro-cracks and grain boundaries. There are several seismic methods that can be used to infer fracture properties in the subsurface; the most common being anisotropic velocity model analysis (e.g., Jones, 2010), amplitude versus offset and azimuth (AVOA) analysis (e.g., Liu & Martinez, 2012) and shear-wave splitting (SWS) analysis (e.g., Savage, 1999). These approaches can infer orientation and density of fractures as well as monitor temporal and spatial variations in fracture properties (e.g., Teanby et al., 2004a).

Although azimuthal variation in velocity and reflection amplitude of P- and S-waves can be diagnostic of anisotropy, shear-wave splitting (SWS) is the least ambiguous indicator of seismic anisotropy. When a shear-wave from an isotropic medium enters an anisotropic region it splits into two orthogonally polarised waves, the S_1-wave will travel faster than the S_2-wave. The degree of splitting depends on the initial S-wave polarisation in the isotropic medium and the allowable polarisation defined by the anisotropic elasticity tensor (e.g., Angus et al., 2004). SWS measures the polarisation direction (ϕ) of the fast S_1-wave and the delay time (δt) between the S_1- and the S_2- waves (e.g., Shearer, 2009). This delay time is proportional to the length of the ray path inside the anisotropic medium and the strength of the seismic anisotropy (e.g., Wuestefeld et al., 2011a). The delay time δt is normalised by the path length between the source and the receiver to yield a percentage difference in S-wave velocity δV_S. There have been several studies that have used SWS results to infer (e.g., Teanby et al., 2004b; Al-Harrasi et al., 2011; Yousef & Angus, 2016) or invert (e.g., Verdon et al., 2009, 2011; Verdon & Wüstefeld, 2013) for various fracture properties, such as fracture density and fracture orientation. SWS inversion techniques use sets of delay times and fast polarisations along with source-to-receiver information such as raypath azimuth, inclination, and travel distance (e.g., Verdon et al., 2009; Wookey, 2012) to image fracture zones and estimate in situ fracture properties.

A significant aspect of the subsurface multi-physical response relates the stiffness of discrete fracture systems. The most common approach for modelling the seismic and geomechanical behaviour of fractured rock is to use an effective medium model (EMM) representation of the fracture network. Although EMM methods have been very useful, there are limitations such as the applicable frequency range, the types of fracture properties which can be studied, and non-uniform influences of, for example, the stress field. The discrete fracture model (DFM) representation is an alternative approach to model fracture networks, where the fractures are considered as discrete or explicit discontinuities. The DFM representation allows relaxing many of the required EMM assumptions and enables the solution to simulate the interaction of seismic waves with fractures systems more accurately, such as modelling the influence of stress state as well as fracture size, fill and stiffness.

In this paper, we study the feasibility of inverting for fracture strike (α) and density (ϵ) for several fracture models having one set of fractures or two sets of orthogonally aligned fractures using microseismic SWS measurements. To do this, we generate a suite of 96 fracture models each for the single and double fracture set geometries with varying fracture size, density, stiffness and effective compliance ratio (we introduce compliance ratio rather than stiffness ratio because it is pervasive in the fracture-induced seismic anisotropy literature). For each model, we generate full-waveform microseismic synthetics using the 3D finite-difference (FD) algorithm WAVE (Hildyard, 2007). The seismic anisotropy induced by the fractures is measured using SWS delay times and fast polarisation directions utilising the approach of Teanby et al. (2004a). Based on an effective medium fracture model, the SWS measurements are inverted for the best fitting fracture model parameters (α and ϵ) using the approach of Verdon & Wüstefeld (2013) and Verdon et al. (2011, 2009). We subsequently compare the inversion results to the true model to evaluate the feasibility of the inversion approach in extracting fracture properties from SWS data.

2. Model

We simulate wave propagation through a suite of elastic models: one subset of models having a single set of aligned fractures and another subset having two orthogonally aligned fracture sets within a homogeneous isotropic medium (Yousef & Angus, 2016, 2017). The background model is isotropic with P-wave velocity of 5700 m/s, S-wave velocity of 3200 m/s and density of 2600 kg/m^3. For each model, a total of 69 3C receivers are used (see Figure 1), with 20 receivers placed in vertical boreholes (four boreholes each containing 5 receivers) and the remaining 49 receivers forming a planar near-surface square array (the near surface array is buried to eliminate free surface noise contamination). The dimension of the elastic model is 300 m$\times$ 300 m $\times$ 300 m. A microseismic source is defined having a Ricker wavelet with dominant frequency of approximation 180 Hz. The source mechanism is a moment tensor having a seismic moment magnitude of 1×10^{14} dyne cm and a strike-slip double-couple mechanism with strike 90°, dip of 90° and slip 45°. To reduce the computational time and allow exploring the influence of fracture properties on the fracture inversion, we simulate one event for each fracture model. In practice, numerous microseismic events would be recorded during microseismic monitoring and so many source-receiver SWS measurements would be used to invert for fracture properties. However, the synthetic data are noise free and so allow studying the feasibility of inverting microseismic SWS for fracture properties.

A total of 96 models have been generated: varying the fracture size a (a= 6, 10, 20 and 50 m), fracture density ϵ (ϵ= 0.02, 0.04, 0.08 and 0.1) and fracture compliance ratio Z_N/Z_T (Z_N/Z_T= 0.33, 0.60 and 1.00) (see Table 1). In this study, fracture density is defined (Hildyard, 2007)

$$\epsilon = \frac{1}{2\pi V} \sum a^3, \tag{1}$$

where V is volume encompassing the fractures, summation is over all discrete fractures within V and the fractures are assumed to be square cracks. The fracture stiffness values are divided into high stiffness models (HS) and low stiffness model (LS). The LS models have values of (1, 5 and 6)$\times 10^{10}$ Pa/m for the normal fracture stiffness K_N and (1, 3 and 2)$\times 10^{10}$ Pa/m for the shear fracture stiffness K_S. Similar values for the HS models have been chosen with the exception that these models have higher stiffness by one order of magnitude. These values were chosen based on the ranges of values observed in the field and laboratory (e.g., Lubbe & Worthington, 2006; Verdon & Wüstefeld, 2013). For the orthogonal double fracture sets, fracture properties are kept identical between the fracture sets to simplify the modelling procedure.

3. SWS results

For all 96 models, a total of 6624 3C seismograms have been processed, where we pick the P- and S-wave arrivals, rotate the 3C seismograms from the global coordinate system (i.e., east, north and vertical) into the local ray (source-receiver) coordinate system (i.e., the ray or P-wave direction and the S_V and S_H directions), and filtered the waveforms using a Butterworth bandpass filter between 10 Hz and 1500 Hz, which is the range of the expected frequencies. After rotation, we calculate the SWS delay time δt and fast polarisation direction (ϕ). After parameter and quality control tests, a P-wave window size of 0.02 s is chosen, where we allow the S-wave window size to vary slightly around 0.01 s (the maximum δt value is constrained to be 3 ms). Next, SWS analysis is performed for each 3C seismogram. For each measurement, a diagnostic plot is created and is used to determine whether a SWS result is good, null or bad. A SWS measurement is classified using an automated quality control value ($\mathbb{Q}$) and is a measure of how similar the SWS measurement parameters of the cross-correlation (XC) and eigenvalue (EV) techniques are (see Wuestefeld et al., 2010, for details). In addition to the automated quality control measure, the SWS measurements can be assessed using the diagnostic plots from the EV method. A SWS measurement is considered reliable by determining whether (1) the energy on the corrected transverse component has been minimised, (2) the S_1- and S_2-waves have similar waveforms, and (3) the elliptical S-wave particle motion in the SV-SH plane has been linearised after the splitting correction. The value of $\mathbb{Q}$ ranges from -1 to +1, where $\mathbb{Q} = -1$ denotes a null result (i.e., no anisotropy and hence no SWS), $\mathbb{Q} = 0$ denoting a poor result (i.e., unreliable) and $\mathbb{Q} = +1$ denoting a good result (i.e., SWS present). We define a $\mathbb{Q}$ value of greater than or equal to 0.75 to be a good SWS result for the synthetic seismograms based on trial and error (i.e., $\mathbb{Q} < 0.75$ resulted in inaccurate fracture inversions). Figure 2 shows an example of a SWS diagnostic plot with a good quality factor ($\mathbb{Q} = 0.96$) and an example of the null result ($\mathbb{Q} = -0.98$). For the good quality factor (Figure 2a) the particle motion is ellipsoidal before correction and is linearised after correction while for the null SWS (Figure 2b) the particle motion is linear before and after the correction.

3.1. Single fracture set vs double fracture sets

For the models having one fracture set, the fracture strike is α=90° from north (i.e., the Y-axis), whereas for the double fracture set models the fracture sets have strike α= 0° and 90° (i.e., the fractures are orthogonal along the X- and Y-axes). Figure 3 depicts the ray coverage in the vertical (inclination) and horizontal (azimuth) planes. There is good azimuth coverage with the exception of a reduction in azimuthal coverage between 210° and 300°. The range of inclination covers mainly between 0° and 60° with some coverage between 60° and 110°. Out of 6624 source-receiver combination there are 445 good SWS measurements ($\approx 7\%$) for the single fracture set models, where as for the double fracture set models there are 261 good SWS measurements ($\approx 4\%$). This is likely due to the presence of the additional fracture set which reduces the amount of coherent scattering that allows SWS to develop (Yousef & Angus, 2016).

Figure 4 is a histogram for azimuth and inclination of the good SWS measurements for the both single and double fracture set models. The figure shows that the majority of the raypaths are between 40° and 120° azimuth travel sub-horizontally through the fracture volume. There is no azimuth coverage between 0° and 40° as well as 140° and 180° since the raypaths do not travel through the fracture volume where SWS would develop. The highest azimuthal counts in the histogram are for the vertical borehole arrays.

Figure 5 shows the distribution of $\mathbb{Q}$ against the difference between initial S-wave polarisation and ϕ in the shear-wave plane (i.e., SV-SH plane). The null measurements can be seen clearly in this figure. Good quality SWS measurements require a separation of at least 20° from the null direction. The scatter reveals that higher $\mathbb{Q}$ values occur when the difference is approximately 45°, and lower $\mathbb{Q}$ values when differences equal to 0° and 90°. This figure confirms the automated quality control approach has a physical basis. However, it would be expected that the signal-to-noise ratio can influence this approach (Wuestefeld et al., 2010). It can be seen for the whole dataset that most of the SWS measurements fall in the category of good null ($\mathbb{Q} < -0.75$). The key point to make is that the SWS quality measure allows for a reduction in the required visual examination of the diagnostic plots (Al-Harrasi et al., 2011). Since the dataset is noise free and the model geometry is designed to maximise S-wave anisotropy, we can automatically control and choose the high SWS measurement quality reliably from the large volume of data. Similarly, Wuestefeld et al. (2010) applied this approach to a Valhall microseismic dataset with the results of the automated SWS analysis being equivalent with the manual results of Teanby et al. (2004b).

To make the SWS less subjective, the $\mathbb{Q}$ value is introduced and is calculated from the combination of both the EV and XC techniques. Both techniques behave differently, particularly in the vicinity of the null direction, where the XC technique fails to extract proper values of ϕ_{XC} and δt_{XC}. This occurs because of the absence or the weakness of S-wave energy on the transverse component close to the null. In fact, correlation can only be found if the rotations of the grid search transfer energy from the initial polarization component to the transverse component. The correlation is maximum for a rotation of 45° and obviously results in zero time lag between the two S-wave components. Therefore, the techniques should not be used alone (Wustefeld & Bokelmann, 2007). The Q value is crucial for reliable fracture inversion of anisotropy measurements; the results of the inversion are dependent on the Q values of the input SWS measurements.

The number of good SWS measurements is a key parameter in the inversion for fracture properties. Based on trial and error and considering the stability of the inversion results for each model, we perform the fracture inversion with a minimum of 5 SWS measurements with $\mathbb{Q} \geq 0.75$, generally leading to a stable inversion. Figure 6 plots the histograms of δt for the whole dataset and good SWS data for both single and double fracture sets. For the whole dataset δt is approximately flat between 0 to 3 ms with higher number of SWS measurements at 0 ms and 3 ms. In contrast, for the good SWS measurements, the δt values the double fracture set models are roughly flat between 0.25 to 2.75 ms and for the single fracture set is similar but with a skewed distribution centred towards lower δt values.

In Figure 7, we plot the published compliance (i.e., inverse stiffness) values versus fracture size a (grey rectangles) from literature (Lubbe, 2005; Pyrak-Nolte et al., 1990; Hardin et al., 1987; Lubbe & Worthington, 2006; King et al., 1986; Worthington & Hudson, 2000) as well as the model values (see table 1) generated in this study. For the three compliance ratios $Z_N/Z_T = 0.33$, 0.60 and 1.00 and fracture sizes a =6, 10, 20 and 50 m the results are categorised into good, unstable and no SWS. The models with good SWS are those that have 5 or more good SWS values $\mathbb{Q} \geq 0.75$ (red), the models with unstable SWS have less than 5 good SWS values (blue) and the models with no SWS (black). The dashed diagonal line in Figure 7 represents the inferred scale dependence of the normal or shear fracture compliance (or stiffness) with fracture size. From Figure 7, it can be observed that by increasing the fracture density ϵ the number of models with good SWS increases, particularly for small fractures. Furthermore, by increasing the compliance Z_N and Z_T (or decreasing stiffness) by one order of magnitude while keeping Z_N/Z_T constant leads to models with good SWS, except for models with fracture size $a = 50$ m and $Z_N/Z_T \geq 0.60$. However, the poor SWS results are due to the fewer number of fractures (i.e., the maximum number is 3) the wave interacts with between source and receivers.

4. EMM inversion method

In this section, the EMM inversion algorithm of (Verdon et al., 2009) is used to invert for fracture strike α and fracture density ϵ. A primary motivation for this study was to assess the key assumption of the inversion approach of Verdon et al. (2009), that the whole path length between source and receiver is fully anisotropic. From a geological perspective, this is unlikely to be a valid assumption. Although minerals are typically anisotropic and that it is recognized that sedimentary layering and fracture systems can induce seismic anisotropy, there must be a coherent fabric over several length scales with respect to the probing seismic wavefield such that anisotropy can develop (e.g., Yousef & Angus, 2016). The measured SWS parameters ϕ and δt are influenced by the path length within an anisotropic volume only, yet directly relating the SWS parameters to the medium elasticity (e.g., strength of anisotropy) requires knowledge of either the fast and slow shear-wave velocity or the path length within the anisotropic volume. In other words, although δt can be used to characterise the strength of anisotropy, there is a trade off in terms of the distance travelled in the anisotropic volume and the strength of the seismic anisotropy. Thus the δt parameter is typically normalised by an assumed path length D to estimate the percentage velocity anisotropy δV_S (i.e., difference between S_1 and S_2 velocity). The δV_S parameter can be computed using the following relationship (e.g., Baird et al., 2013):

$$\delta V_S = 100 \frac{V_{S1} - V_{S2}}{(V_{S1} + V_{S2})/2}, \tag{2}$$

where t is the traveltime and $V_{S1} = D/t$ is velocity of the fast S-wave, and $V_{S2} = D/(t + \delta t)$ is the velocity of the slow S-wave. For the results in this study and assuming the full raypath is within an anisotropic volume, the maximum S-wave velocity anisotropy δV_S for the single and double fracture sets are approximately 16% and 21%, respectively.

To obtain reliable inversion results, the inversion is performed for models with at least 5 good SWS results ($\mathbb{Q} \geqslant 0.75$). To assess the inversion approach, we first invert for the fracture properties of the single vertical fracture set models, which represent a simpler model and hence, in principle, a more constrained inversion. Subsequently, we then invert for fracture properties of the orthogonal fracture set models (orthorhombic model). The algorithm allows for the inversion for background VTI anisotropy (e.g., Verdon et al., 2011), but since the background medium is isotropic the anisotropy parameters are excluded from the inversion process. Therefore, the independent parameters in the inversion are fracture strike and fracture density for the single and double fracture set models.

We should note that the EMM inversion uses an effective fracture compliance (B_N, B_T with unit Pa^{-1}) as a representation of the whole discrete fracture volume rather than individual fracture compliance (Z_N, Z_T with unit m Pa^{-1}). Unlike B_N and B_T, that describe the equivalent medium compliance of a full fracture set and have dimension 1/stress (Pa^{-1}), Z_N and Z_T are compliances of the individual discrete fracture with dimension length/stress (m/Pa). The $Z_{(N,T)}$ and $B_{(N,T)}$ can be related thorough the following equation

$$B_{(N,T)} = \frac{Z_{(N,T)}}{H}, \tag{3}$$

where H is the average fracture spacing in a direction normal to the fracture surface (Worthington, 2008).

In order to obtain the optimum estimates of fracture strike and fracture density and also minimise the computation time of the inversion, we limit the grid search to sensible values for these parameters. For the single fracture inversion, we allow α to vary between 0° and 180°, whereas for the double fracture inversion, we allow $\alpha1$ and $\alpha2$ to vary between $\alpha1$ =-45° and 45° and $\alpha2$ = 45° and 135° for the first and second fracture sets. Following the assumption of Crampin (1994) that fracture density is roughly equal to one hundredth of δV_S and assuming a maximum δV_S of 21%, we set the fracture density range to be between 0.00 and 0.14 for both the single and double fracture sets.

5. Results

5.1. Single fracture set

Figure 8 shows the inversion results for α and ϵ for the single fracture set models as a polar plot diagram. The inverted fracture strikes fall within $\pm 40°$ of the true model fracture strike $\alpha = 90°$. The inverted strikes for the $Z_N/Z_T = 0.60$ are more tightly constrained around the true model. The average and standard deviation of the inversion results for the three categories of compliance ratio Z_N/Z_T are given in Table 3. A general observation from the inversion results of the single fracture models suggests that fracture strike is much better constrained than fracture density, consistent with the results of Verdon et al. (2011); Yousef & Angus (2016).

5.2. Double fracture sets

Figure 9 shows the inversion results for fracture strike ($\alpha 1$ and $\alpha 2$) and fracture density ($\epsilon 1$ and $\epsilon 2$) for the double fracture set models. The results reveal that the inverted fracture strike and density for fracture set 2 are better constrained than those for fracture set 1. The inverted fracture strikes are close to the true model fracture strikes (i.e., 0° and 90°), indicating that the inversion for strike has been successful. However, the inverted fracture densities are less accurate when the fracture sets are orthogonal. This finding is consistent with the inverted fracture densities of Verdon et al. (2009). Furthermore, Grechka & Tsvankin (2003) have discussed that it is possible for a broad range of fracture density models to produce an equivalent effective medium stiffness tensor. Table 4 lists the average errors in the inversion for fracture strike and density for both fracture sets for each compliance ratio Z_N/Z_T. Since the fractures in the model are orthogonal, we examine the orthogonality of the inverted fracture strikes. Figure 10 shows a polar plot diagram of the difference in strike between the inverted fracture strikes $\Delta\alpha$. The plot reveals that the majority of the inversions have $\Delta\alpha = 90° \pm 30°$. From Figure 10 it can be observed that the inversion results for fracture densities versus $\Delta\alpha$ are better constrained with increasing compliance ratio Z_N/Z_T.

Figure 11 presents the inverted fracture strike versus fracture density for both single and double fracture set models. From this figure, it is apparent that the maximum strike inversion error for the single fracture set models (i.e., 80°) is approximately double of those results for the double fracture set. In contrast, the inversion error for fracture density for both single and double fracture set models are generally between 40% and 100%.

6. Discussion

From Figures 8 to 9 it can be observed that the inversion algorithm is capable of estimating fracture strike without prior knowledge of the medium fracture properties. The outliers are likely influenced by the non-linear nature of the inversion algorithm and the fact that the inversion uses only a single event to characterise a finite fracture volume. Furthermore, the location of the source and orientation of failure source mechanism may be insufficient to illuminate the fracture set. However, with more sources spatially distributed around the fracture volume and more favourable (i.e, more data) it is possible that the fracture inversion would yield more accurate results (Rial et al., 2005). For the double fracture set models, the inverted strike for the 0° fracture set degrades, whereas the inverted strike for the 90° fracture set appears to be better resolved (broader but fewer outliers). Improvements on resolving strike can be made by including more microseismic sources in the inversion process.

In contrast, it should be noted that the inverted fracture densities are systematically underestimated from the true value for the single fracture set (i.e., the inversion results clustered between 0.00 and 0.06), while it is systematically overestimated for the double fracture sets for the low compliance ratios (i.e., $Z_N/Z_T = 0.33$ and 0.60). This seems to be mainly caused by the both fracture densities in the real model being constant and secondly, a trade-off between the two fracture densities that is inherent in the inversion as noted by Verdon et al. (2011). More importantly, the EMM inversion algorithm assumes that the whole medium in which the ray traverses is fractured, instead of only a portion of the raypath within fracture zone. This is likely the main cause of the poor estimates of fracture density. Improvements in resolving fracture density (or stiffness) can be achieved using a more advanced inversion approach such as anisotropic tomography in which the medium can divided into different domains with each domain having different anisotropic characteristics (e.g., Abt & Fischer, 2008; Wookey, 2012). However, Yousef & Angus (2016) show that the inaccurate estimates of fracture density is influenced also by the choice of effective medium rock physics model. For this study, the inadequacy of the linear-slip model is a contributing factor in the poor estimates of fracture density (e.g., Yousef & Angus, 2016).

7. Conclusions

We have shown that it is feasible to invert SWS measurements to quantitatively estimate fracture strike and fracture density assuming an effective medium fracture model. The results of the full waveform FD synthetics indicate that the source frequency of the microseismicity will be crucial in extracting reliable fracture parameters due to the relationship between scale length of the probing seismic wave and the fracture heterogeneity (i.e., size). Although the SWS results themselves are diagnostic of fracturing, the fracture inversion allows placing constraints on the physical properties of the fracture system. For real microseismic datasets, the range in magnitude of microseismicity (i.e., frequency content), spatial distribution and variable source mechanisms suggests that the inversion of fracture properties from SWS measurements is feasible. For the single seismic source case and optimum receiver array geometry, the inversion for strike has average errors of between 11° and 25°, whereas for density has average errors between 65% and 80% for the single fracture set and 30% and 90% for the double fracture sets.

Acknowlegments

B. Yousef would like to acknowledge Kurdistan regional government for their financial support of his PhD study. D. Angus acknowledges the Research Council UK (EP/K035878/1; EP/K021869/1; NE/L000423/1) and M. Hildyard acknowledges the Research Council UK (NE/L000423/1) for financial support.

References

Abt, D. L., & Fischer, K. M. (2008). Resolving three-dimensional anisotropic structure with shear wave splitting tomography. *Geophysical Journal International*, *173*, 859–886.

Al-Harrasi, O., Al-Anboori, A., Wüstefeld, A., & Kendall, J. M. (2011). Seismic anisotropy in a hydrocarbon field estimated from microseismic data. *Geophysical Prospecting*, *59*, 227–243.

Angus, D. A., Thomson, C. J., & Pratt, R. G. (2004). A one-way wave equation for modelling variations in seismic waveforms due to elastic anisotropy. *Geophysical Journal International*, *156*, 595–614.

Baird, A. F., Kendall, J.-M., & Angus, D. A. (2013). Frequency-dependent seismic anisotropy due to fractures: Fluid flow versus scattering. *Geophysics*, *78*, WA111–WA122.

Crampin, S. (1994). The fracture criticality of crustal rocks. *Geophysical Journal International*, *118*, 428–438.

Grechka, V., & Tsvankin, I. (2003). Feasibility of seismic characterization of multiple fracture sets. *Geophysics*, *68*, 1399–1407.

Hardin, E., Cheng, C., Paillet, F., & Mendelson, J. (1987). Fracture characterization by means of attenuation and generation of tube waves in fractured crystalline rock at mirror lake, new hampshire. *Journal of Geophysical Research: Solid Earth (1978–2012)*, *92*, 7989–8006.

Hildyard, M. (2007). Manuel rocha medal recipient wave interaction with underground openings in fractured rock. *Rock Mechanics and Rock Engineering*, *40*, 531–561.

Jones, I. F. (2010). *An Introduction to Velocity Model Building*. EAGE.

King, M. S., Myer, L. R., & Rezowalli, J. J. (1986). Experimental studies of elastic-wave propagation in a columnar-jointed rock mass. *Geophysical Prospecting*, *34*, 1185–1199.

Liu, E., & Martinez, A. (2012). Seismic fracture characterization: Concepts and practical applications, . (p. 280).

Lubbe, R. (2005). A field and laboratory investigation of the compliance of fractured rock. *DPhil thesis*, *Oxford University*.

Lubbe, R., & Worthington, M. H. (2006). A field investigation of fracture compliance. *Geophysical Prospecting*, *54*, 319–331.

Pyrak-Nolte, L. J., Myer, L. R., & Cook, N. G. W. (1990). Anisotropy in siesmic velocities and amplitudes from multiple parallel fractures. *Journal of Geophysical Research-Solid Earth and Planets*, *95*, 11345–11358.

Rial, J. A., Elkibbi, M., & Yang, M. (2005). Shear-wave splitting as a tool for the characterization of geothermal fractured reservoirs: lessons learned. *Geothermics*, *34*, 365–385.

Savage, M. (1999). Seismic anisotropy and mantle deformation: What have we learned from shear wave splitting? *Reviews Of Geophysics*, *37*, 65–106.

Shearer, P. M. (2009). *Introduction to seismology*. Cambridge University Press.

Teanby, N., Kendall, J.-M., & Van der Baan, M. (2004a). Automation of shear-wave splitting measurements using cluster analysis. *Bulletin of the Seismological Society of America*, *94*, 453–463.

Teanby, N., Kendall, J.-M., Jones, R., & Barkved, O. (2004b). Stress-induced temporal variations in seismic anisotropy observed in microseismic data. *Geophysical Journal International*, *156*, 459–466.

Verdon, J., Kendall, J.-M., & Wüstefeld, A. (2009). Imaging fractures and sedimentary fabrics using shear wave splitting measurements made on passive seismic data. *Geophysical Journal International*, *179*, 1245–1254.

Verdon, J. P., Kendall, J. et al. (2011). Detection of multiple fracture sets using observations of shear-wave splitting in microseismic data. *Geophysical Prospecting*, *59*, 593–608.

Verdon, J. P., & Wüstefeld, A. (2013). Measurement of the normal/tangential fracture compliance ratio (zn/zt) during hydraulic fracture stimulation using s-wave splitting data. *Geophysical Prospecting*, *61*, 461–475.

Wookey, J. (2012). Direct probabilistic inversion of shear wave data for seismic anisotropy. *Geophysical Journal International*, *189*, 1025–1037.

Worthington, M. (2008). Interpreting seismic anisotropy in fractured reservoirs. *First Break*, *26*.

Worthington, M., & Hudson, J. (2000). Fault properties from seismic q. *Geophysical Journal International*, *143*, 937–944.

Wuestefeld, A., Al-Harrasi, O., Verdon, J. P., Wookey, J., & Kendall, J. M. (2010). A strategy for automated analysis of passive microseismic data to image seismic anisotropy and fracture characteristics. *Geophysical Prospecting*, *58*, 755–773.

Wuestefeld, A., Verdon, J. P., Kendall, J.-M., Rutledge, J., Clarke, H., & Wookey, J. (2011a). Inferring rock fracture evolution during reservoir stimulation from seismic anisotropy. *Geophysics*, *76*, WC157–WC166.

Wustefeld, A., & Bokelmann, G. (2007). Null detection in shear-wave splitting measurements. *Bulletin of the Seismological Society of America*, *97*, 1204–1211.

Yousef, B. M., & Angus, D. A. (2016). When do fractured media become seismically anisotropic? some implications on quantifying fracture properties. *Earth and Planetary Science Letters*, *444*, 150–159.

Yousef, B. M., & Angus, D. A. (2017). Analysis of fracture induced scattering of microseismic shear-waves. *Studia Geophysica et Geodaetica*, *61*, 26.

$Z_N/Z_T = 0.33$								
Fracture density	0.02		0.04		0.08		0.1	
size (m)	K_N	K_T	K_N	K_T	K_N	K_T	K_N	K_T
6	6×10^{10}	2×10^{10}	6×10^{10}	2×10^{10}	6×10^{10}	2×10^{10}	6×10^{10}	2×10^{10}
6	6×10^{11}	2×10^{11}	6×10^{11}	2×10^{11}	6×10^{11}	2×10^{11}	6×10^{11}	2×10^{11}
10	3×10^{10}	1×10^{10}	3×10^{10}	1×10^{10}	3×10^{10}	1×10^{10}	3×10^{10}	1×10^{10}
10	3×10^{11}	1×10^{11}	3×10^{11}	1×10^{11}	3×10^{11}	1×10^{11}	3×10^{11}	1×10^{11}
20	3×10^{9}	1×10^{9}	3×10^{9}	1×10^{9}	3×10^{9}	1×10^{9}	3×10^{9}	1×10^{9}
20	3×10^{10}	1×10^{10}	3×10^{10}	1×10^{10}	3×10^{10}	1×10^{10}	3×10^{10}	1×10^{10}
50	3×10^{9}	1×10^{9}	3×10^{9}	1×10^{9}	3×10^{9}	1×10^{9}	3×10^{9}	1×10^{9}
50	3×10^{10}	1×10^{10}	3×10^{10}	1×10^{10}	3×10^{10}	1×10^{10}	3×10^{10}	1×10^{10}
$Z_N/Z_T = 0.6$								
Fracture density	0.02		0.04		0.08		0.1	
size (m)	K_N	K_T	K_N	K_T	K_N	K_T	K_N	K_T
6	5×10^{10}	3×10^{10}	5×10^{10}	3×10^{10}	5×10^{10}	3×10^{10}	5×10^{10}	3×10^{10}
6	5×10^{11}	3×10^{11}	5×10^{11}	3×10^{11}	5×10^{11}	3×10^{11}	5×10^{11}	3×10^{11}
10	5×10^{10}	3×10^{10}	5×10^{10}	3×10^{10}	5×10^{10}	3×10^{10}	5×10^{10}	3×10^{10}
10	5×10^{11}	3×10^{11}	5×10^{11}	3×10^{11}	5×10^{11}	3×10^{11}	5×10^{11}	3×10^{11}
20	5×10^{9}	3×10^{9}	5×10^{9}	3×10^{9}	5×10^{9}	3×10^{9}	5×10^{9}	3×10^{9}
20	5×10^{10}	3×10^{10}	5×10^{10}	3×10^{10}	5×10^{10}	3×10^{10}	5×10^{10}	3×10^{10}
50	5×10^{9}	3×10^{9}	5×10^{9}	3×10^{9}	5×10^{9}	3×10^{9}	5×10^{9}	3×10^{9}
50	5×10^{10}	3×10^{10}	5×10^{10}	3×10^{10}	5×10^{10}	3×10^{10}	5×10^{10}	3×10^{10}
$Z_N/Z_T = 1.0$								
Fracture density	0.02		0.04		0.08		0.1	
size (m)	K_N	K_T	K_N	K_T	K_N	K_T	K_N	K_T
6	1×10^{10}	1×10^{10}	1×10^{10}	1×10^{10}	1×10^{10}	1×10^{10}	1×10^{10}	1×10^{10}
6	1×10^{11}	1×10^{11}	1×10^{11}	1×10^{11}	1×10^{11}	1×10^{11}	1×10^{11}	1×10^{11}
10	3×10^{10}	3×10^{10}	3×10^{10}	3×10^{10}	3×10^{10}	3×10^{10}	3×10^{10}	3×10^{10}
10	3×10^{11}	3×10^{11}	3×10^{11}	3×10^{11}	3×10^{11}	3×10^{11}	3×10^{11}	3×10^{11}
20	1×10^{9}	1×10^{9}	1×10^{9}	1×10^{9}	1×10^{9}	1×10^{9}	1×10^{9}	1×10^{9}
20	1×10^{10}	1×10^{10}	1×10^{10}	1×10^{10}	1×10^{10}	1×10^{10}	1×10^{10}	1×10^{10}
50	3×10^{9}	3×10^{9}	3×10^{9}	3×10^{9}	3×10^{9}	3×10^{9}	3×10^{9}	3×10^{9}
50	3×10^{10}	3×10^{10}	3×10^{10}	3×10^{10}	3×10^{10}	3×10^{10}	3×10^{10}	3×10^{10}

Table 1: Summary of fracture properties for all models, where K_N and K_T are in units Pa/m.

Z_N/Z_T	0.33	0.6	1.0
$\Delta\epsilon$	70 ± 23	66.55 ± 27.52	68.69 ± 15.59
$\Delta\alpha$	23.02 ± 16.82	14 ± 17.24	10.57 ± 8.92

Table 2: Average fracture and density inversion error for the single fracture set models.

Z_N/Z_T	$\Delta\epsilon(\%)$	$\Delta\alpha(^\circ)$
0.33	76.85 ± 41.62	24.00 ± 21.53
0.6	66.56 ± 25.74	16.19 ± 23.95
1.0	67.79 ± 16.36	11.40 ± 8.75

Table 3: Average error in fracture strike and density for the single fracture set models (given as average error $\pm$ standard deviation).

Z_N/Z_T	$\Delta\epsilon1(\%)$	$\Delta\alpha1(^\circ)$	$\Delta\epsilon2(\%)$	$\Delta\alpha2(^\circ)$
0.33	88.38 ± 101.62	23.41 ± 13.73	60.21 ± 61.95	22.68±11.97
0.6	67.61 ±76.84	14.68±9.78	31.64±38.04	15.88±12.39
1.0	40.83±11.24	21.37±16.93	60.08±4.57	21.39±15.15

Table 4: Average error in fracture strike and density error for the double fracture set models (given as average error ± standard deviation).

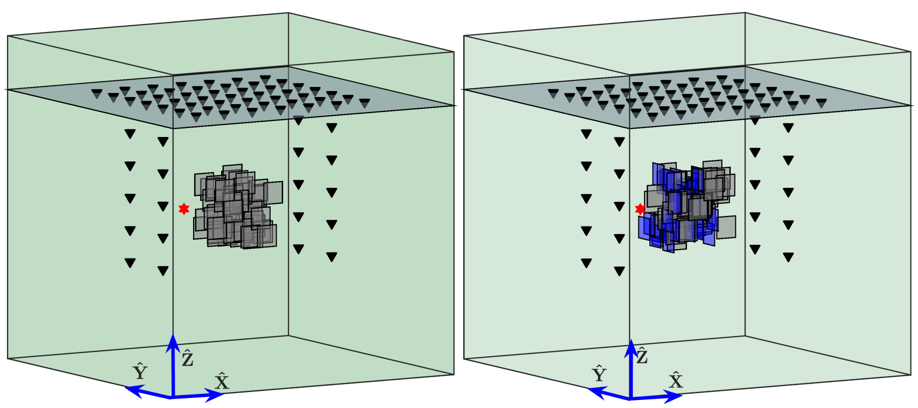

(a) (b)

Figure 1: Geometry of the 3D FD model with (a) one set of aligned fractures and (b) two sets of aligned fractures. The red star represents the location of the micro-seismic source (located in the centre of the left edge of the fracture zone), the triangles represent the surface and borehole receivers and the grey and blue rectangles within the sub-volume schematically represent the vertical fractures.

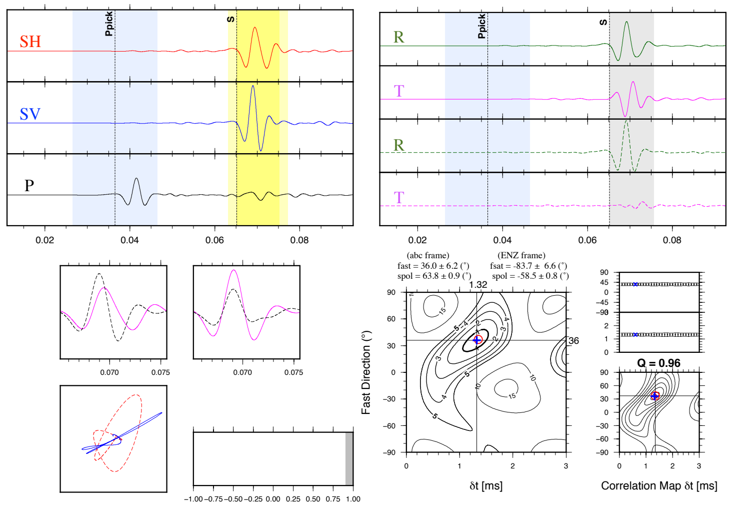

(a)

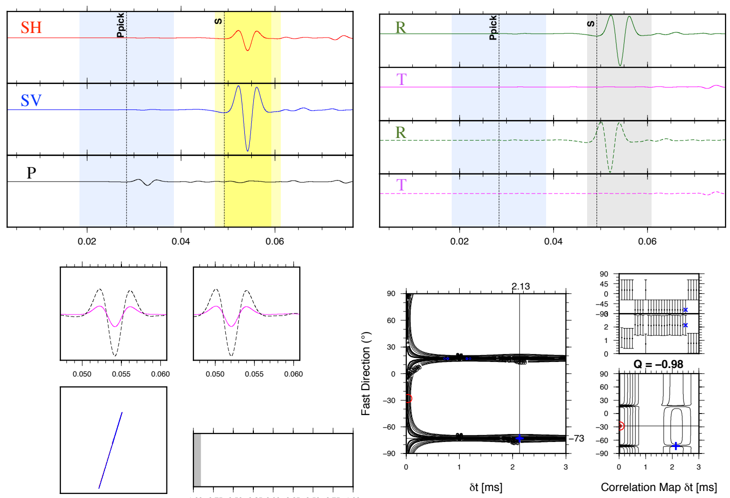

(b)

Figure 2: Example of (a) good SWS measurement ($\mathbb{Q} = 0.96$) and (b) null splitting ($\mathbb{Q} = -0.98$). For (a) and (b); (top-left) 3 component waveforms in local ray coordinates; (top-right) radial and transverse components before (top 2 traces) and after (bottom 2 traces) splitting correction; (middle-left) fast (dashed) and slow (solid) S waves before (left) and after (right) correction; (bottom-left) particle motion in SV-SH coordinate frame before (dashed) and after (solid) correction; (bottom-right) error surfaces of the eigenvalue (left) and cross-correlation (lower right) methods (see Wuestefeld et al., 2010, for details). The best result of the two methods are shown as blue + and red circle for the eigenvalue and cross-correlation method, respectively; and (middle-right) fast axis (top) and δt variations for each window including corresponding error bars.

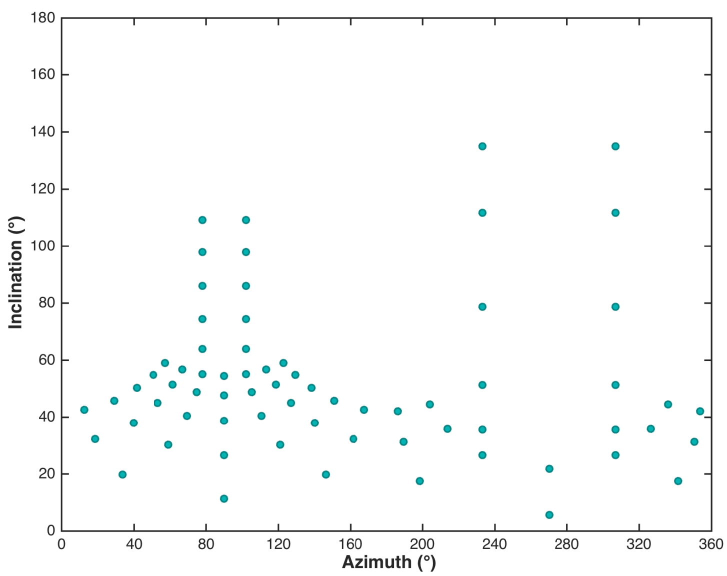

Figure 3: Distribution of source-receiver azimuth and inclination for the fracture model array.

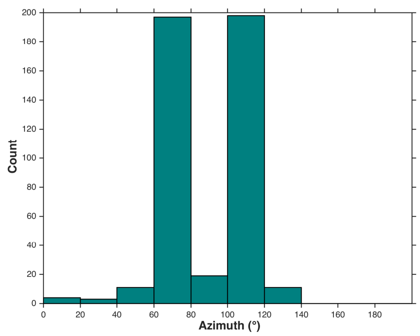

(a) Single fracture

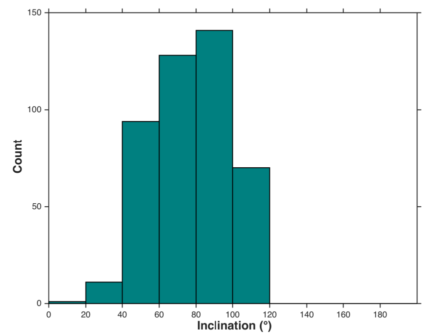

(b) Single fracture

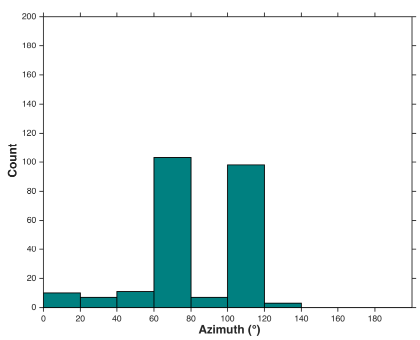

(c) Double fracture

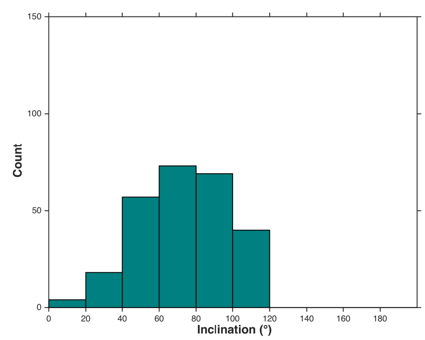

(d) Double fracture

Figure 4: Histogram of azimuth and inclination of the good SWS for the single and double fracture sets.

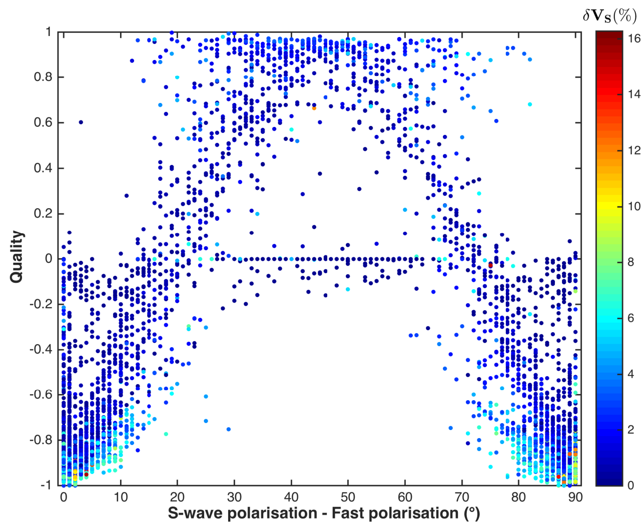

(a) Single fracture

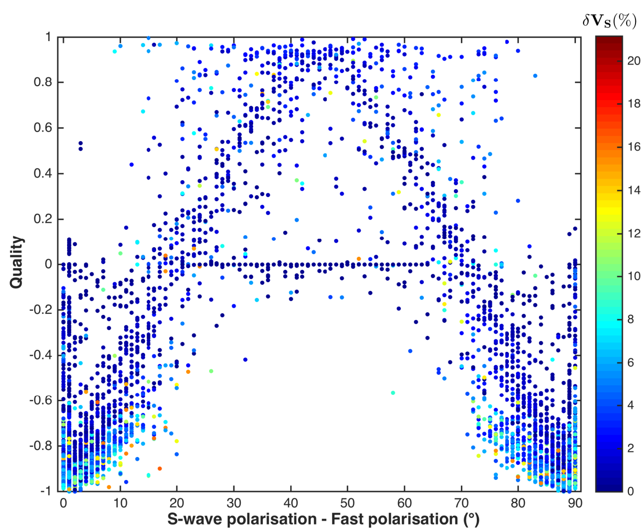

(b) Double fracture

Figure 5: The SWS quality versus difference between initial source polarisation and the fast S-wave polarisation (ϕ) in the S-plane for the whole dataset. The colour depicts the percentage of shear-wave splitting δV_S. Note that the colour scales are not normalised between the two models.

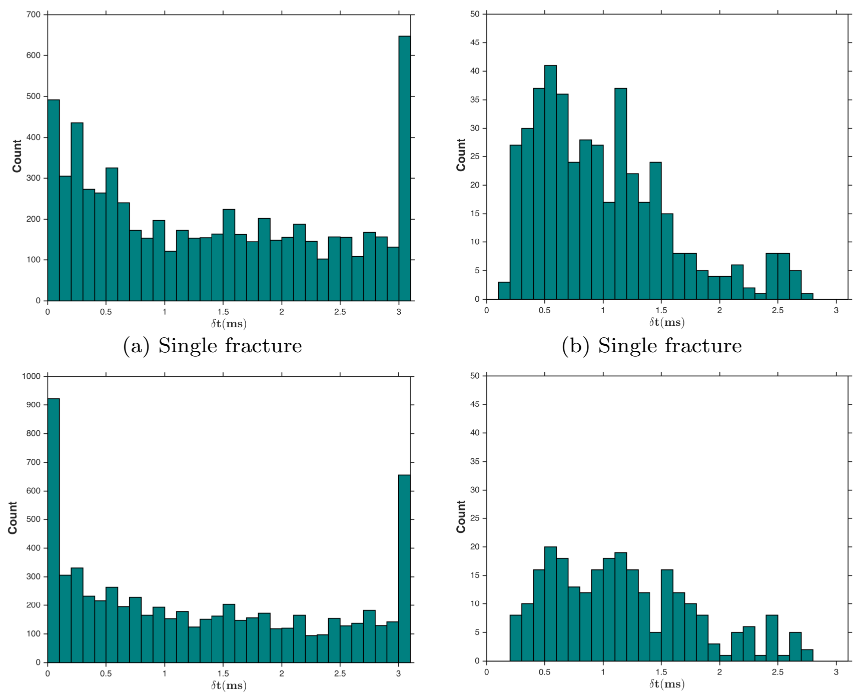

(a) Single fracture

(b) Single fracture

(c) Double fracture

(d) Double fracture

Figure 6: Histogram of δt for the whole dataset for the single (a) and double (c) fracture set models (6624 measurements) as well as for the good SWS results $\mathbb{Q} \geq 0.75$) for the single (b) and double (d) fracture set models. .

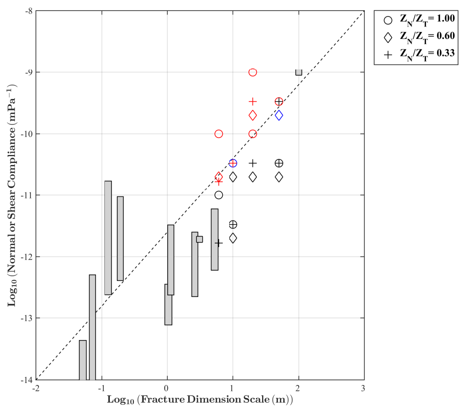

(a) $\epsilon = 0.02$

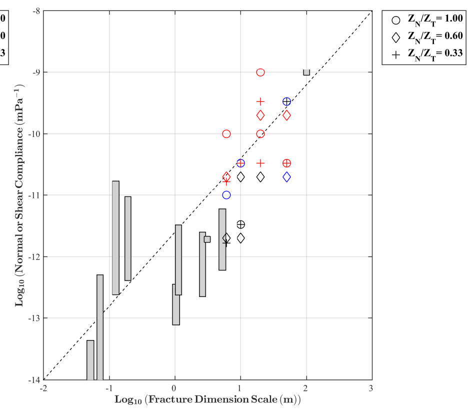

(b) $\epsilon = 0.04$

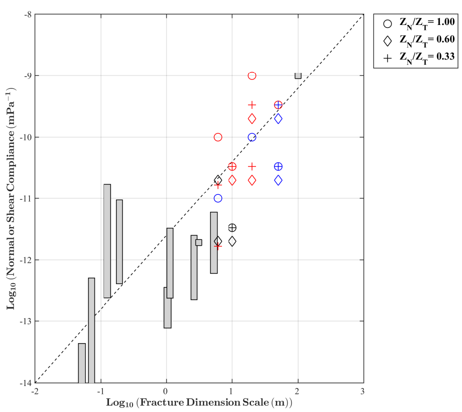

(c) $\epsilon = 0.08$

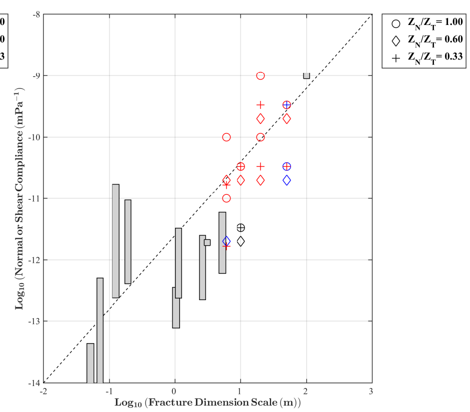

(d) $\epsilon = 0.1$

Figure 7: Normal compliance (i.e., inverse stiffness) against fracture size. The grey rectangles are data taken from literature while the other symbols are data from this study. The colour depicts the quality of SWS: good (red); unstable (blue); no SWS (black).

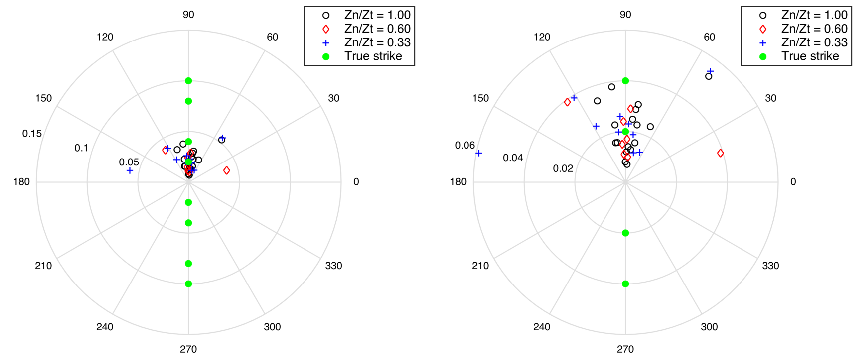

(a) (b)

Figure 8: Inversion results for fracture strike versus fracture density for the single fracture set models in the polar plot diagram (left) and zoom in for clear visualisation of the results (right).

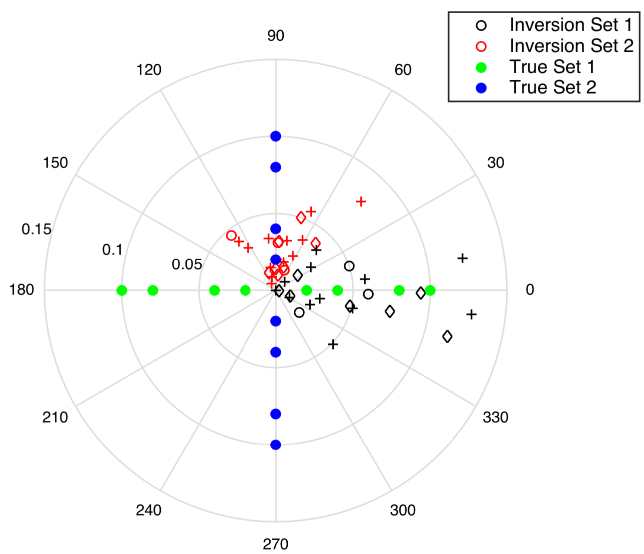

Figure 9: Inversion results for fracture strike versus fracture density for the double fracture set models in polar diagram.

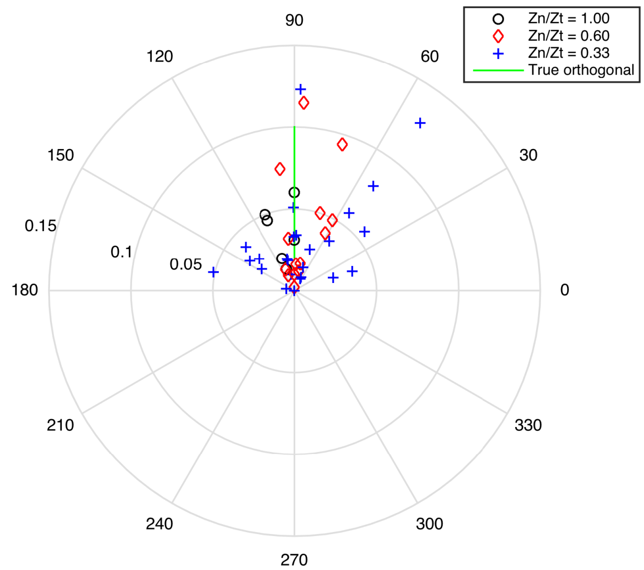

Figure 10: The results of difference in fracture strike inversion for the double fracture sets of in the polar coordinate for the Z_N/Z_T=1.00, 0.60 and 0.33. The radial axis and the angular axes are the fracture density and fracture strike respectively.

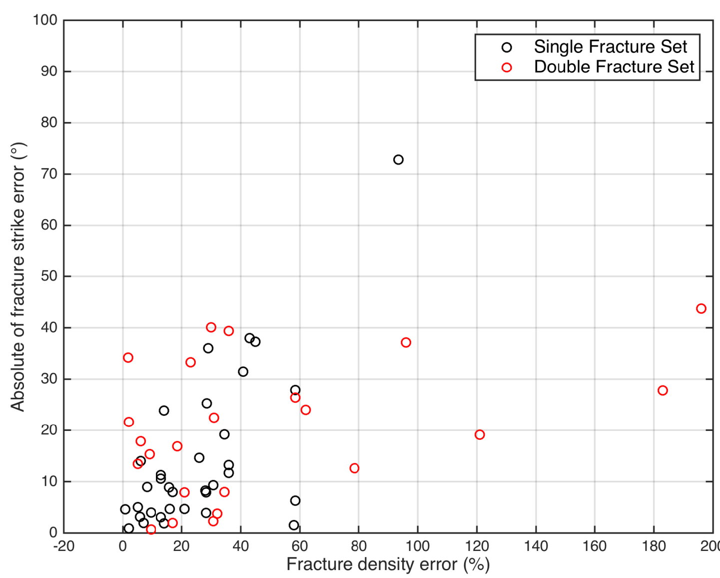

Figure 11: Comparison of inversion results for fracture strike versus fracture density for both the single and double fracture set models.